Registration of Pre- and Post-resection Ultrasound Volumes with Non-corresponding Regions in Neurosurgery

Hang Zhou, *Student Member, IEEE,* Hassan Rivaz, *Member, IEEE*

This paper is among the 10 papers selected for publication in JBHI (out of 2,498 submissions to IEEE EMBC).

***Abstract*—Brain tissue deforms significantly after opening the dura and during tumor resection, invalidating pre-operative imaging data. Ultrasound is a popular imaging modality for providing the neurosurgeon with real-time updated images of brain tissue. Interpretation of post-resection ultrasound images is difficult due to large brain shift and tissue resection. Furthermore, several factors degrade the quality of post-resection ultrasound images such as the strong reflection of waves at the interface of saline water and brain tissue in resection cavities, air bubbles and the application of blood-clotting agents around the edges of resection. Image registration allows the comparison of post-resection ultrasound images with higher quality pre-resection images, assists in interpretation of post-resection images and may help identify residual tumor, and as such, is of significant clinical importance. In this paper, we propose a nonrigid symmetric registration (NSR) framework for accurate alignment of pre- and post-resection volumetric ultrasound images in near real-time. We first formulate registration as minimization of a regularized cost function, and analytically derive its derivative to efficiently optimize the cost function. An outlier detection algorithm is proposed and utilized in this framework to identify non-corresponding regions (outliers) and therefore improve the robustness and accuracy of registration. We use an Efficient Second-order Minimization (ESM) method for fast and robust optimization. Furthermore, we exploit a symmetric and inverse-consistent method to generate realistic deformation fields. The results show that NSR significantly improves the quality of the alignment between pre- and post-resection ultrasound images.**

***Index Terms*—Efficient Second-order Minimization (ESM), Image Registration, Neurosurgery, Outlier Detection, Ultrasound Imaging**

I. Introduction

THE problem of residual tumor has attracted serious concern in tumor surgery. The infiltrating nature of brain tumors and the possibility of causing cognitive deficit to the patient after the resection of critical parts lead to residual tumor in as much as 64% of patients [1]. Therefore, neuro-navigation systems are commonly used in many sites where image-to-patient registration is performed by selecting corresponding landmarks in the pre-operative magnetic resonance (MR) image and on the skin. Unfortunately, this registration is inaccurate for two main reasons. First, brain tissue deforms during surgery and after craniotomy as much as 50 mm [2], which renders pre-operative MR images inaccurate. Second, the selection of corresponding landmarks on the skin and in the MR image is inaccurate, and leads to large registration errors. To allow the visualization of the brain during surgery, intra-operative MR has been used. However, intra-operative MR is extremely expensive and requires dedicated operation rooms as well as MR compatible equipment, which hinder its wide application in surgical operations.

Alternatively, intra-operative ultrasound imaging is convenient and significantly less expensive, and as such, is used in many neurological centers. An ultrasound volume is obtained before tumor resection to allow the visualization of tumor boundaries and critical brain structures. More ultrasound scans are acquired during and after resection to help the surgeon locate and minimize residual tumor. Unsgård *et al.* [3] and Solheim *et al.* [4] demonstrated the significance of intra-operative ultrasound imaging in neurosurgery based on more than 900 operations. El Beltagy *et al.* [5] collected pre-, during and post-resection ultrasound images, as well as MR images before and immediately (within 48 h) after surgery, and concluded that intra-operative ultrasound was useful in identifying tumor boundaries and minimizing residual tumor. Recently, Renovanz *et al.* [6], Petridis *et al.* [7], Coburger *et al.* [8] and Moiyadi & Shetty [9] performed a retrospective analysis of the Gross-Total Resection (GTR) of patients who underwent ultrasound guided neurosurgery and concluded that ultrasound could be effective in achieving GTR, especially for low-grade glioma.

It is generally more difficult for neurosurgeons to interpret post-operative ultrasound images due to resection of tissue and large brain shift. In addition, the large difference in acoustic impedance between the saline water solution, as well as the blood clotting agent that is placed around resection cavities create strong reflection at the boundary of resection. This strong reflection can overshadow possible residual tumor in post-resection ultrasound images. In Selbekk *et al.* [10], different underlying reasons of image artifacts and their impact on the quality of ultrasound images were demonstrated, and a novel acoustic coupling fluid method was proposed to reduce these artifacts.

Registration of pre- and post-operation ultrasound volumes is of significant clinical interest: it simplifies interpretation of post-resection images, and may help in identifying residual tumor. This registration is challenging for several reasons. First, both the deformation and imaging data are in 3D, entailing computationally demanding 3D calculations. Second,

Hang Zhou is with the Department of Electrical and Computer Engineering and PERFORM Center, Concordia University, Montreal, Quebec, Canada e-mail:z_hang@encs.concordia.ca

Hassan Rivaz is with the Department of Electrical and Computer Engineering and PERFORM Center, Concordia University, Montreal, Quebec, Canada e-mail:hrivaz@ece.concordia.ca

shadowing and enhancing, which are well-known artifacts in ultrasound imaging [11], are common in post-resection images. Therefore, the intensity of the same tissue can be very different in pre- and post-resection ultrasound volumes. Finally, because of the removal of partial tissue during resection, some regions of pre- and post-resection images do not correspond to each other.

Registration of ultrasound volumes is an active field of research with numerous new advances. Ultrasound registration methods can be categorized into feature-based [12], [13], [14] and intensity-based [15], [16], [17], [18], [19]. Feature-based methods first find corresponding points in the two ultrasound volumes, and then use these correspondences to find the registration transformation. Intensity-based methods rely on similarity metrics such as Normalized Cross Correlation (NCC) [16], [17], [19], mutual information [18], or phase differences [15]. Another categorization can be made based on the transformation, which can be rigid [15], [16], [13], [18], [19] or deformable [12], [17], [14]. Deformable registration usually has significantly more degrees of freedom, and is therefore more challenging.

The detection of non-corresponding regions is another area of related work. Banerjee *et al.* [20] performed affine registration between two volumes to compensate for the motion of liver, while outliers were detected and rejected with a novel outlier rejection algorithm based on a geometric consistency term. Gao *et al.* [21] developed a probabilistic and outlier-adaptive algorithm using an Expectation Maximization (EM) framework wherein the ratio of outlier data was updated in every iteration. Khamene *et al.* [22] first obtained a prior intensity distribution of non-corresponding regions in the training step. In the registration step, the transformations that mapped the intensity distribution of outlier regions to the prior distribution were favored.

A closely related work registered pre- and post-resection ultrasound images of neurosurgery by first performing manual segmentation of resection cavities [17]. Another related technique called RESOUND [23] was based on gradient descent optimization of a regularized cost function with deformable free-form B-splines transformation. An important issue with RESOUND, however, is that free-form B-splines are not invertible and can generate folds and ruptures that are physically unrealistic. Another issue lies in the optimization scheme used in RESOUND, which is based on gradient descent and therefore has a linear convergence rate. This can hinder the clinical application of RESOUND where robust and accurate performance is critical.

In this work, we build on RESOUND and propose a novel robust deformable registration technique for the alignment of pre- and post-resection ultrasound images called Nonrigid Symmetric Registration (NSR). Two main contributions of this work are as follows: 1) We incorporate symmetric deformation fields that are invertible and an Efficient Second-order Minimization (ESM) method [24] into our registration technique to create high quality deformation fields while maintaining a fast and reliable convergence. To the best of our knowledge, this is the first time symmetric deformation and ESM are used in ultrasound registration. 2) We propose an accurate outlier detection approach and validate its effectiveness on both simulated images and clinical data. We evaluate our framework on ultrasound images of 13 patients quantitatively and qualitatively, and demonstrate that NSR detects non-corresponding regions and registers these challenging images accurately and efficiently. A shorter version of this paper was recently published in [25].

II. Methods

A. Deformation

Numerous registration algorithms, including RESOUND, find a nonrigid transformation that maps one image to another. Several issues arise in such registration framework: the resulting transformation is not symmetric with respect to the two images, and therefore is biased on the selection of the moving image domain. Also, the deformation is not necessarily invertible, and can cause physically implausible folds or ruptures. To overcome these problems, inverse-consistent registration methods have been proposed in [26], [27]. They reduce bias by calculating forward and backward transformations $\mathbf{T_1}$ and $\mathbf{T_2}$, and penalize the difference between $\mathbf{T_1} \circ \mathbf{T_2}$ and the identity transformation. In this work, we utilize a symmetric and inverse-consistent method similar to [28], and apply the iterative approach of [29] to invert transformations. Full forward and backward deformation can then be calculated as $\mathbf{T_1}(0.5) \circ \mathbf{T_2}(0.5)^{-1}$ and $\mathbf{T_2}(0.5) \circ \mathbf{T_1}(0.5)^{-1}$ respectively, where 0.5 means half of the deformation field and $\circ$ represents composition of transformations.

The outline of our registration framework is shown in Fig. 1. Let $\mathbf{V_1}$ and $\mathbf{V_2}$ represent two ultrasound volumes, and $\mathbf{x} \subset R_d$ denote global coordinates, where $d = 3$ for 3D volumetric images. Also, $\mathbf{T_u}(\mathbf{x}) = \mathbf{x} + \mathbf{u}$ represents forward and backward deformations. The goal of our registration framework is to find the 3D deformation fields $\mathbf{u_1}$ from $\mathbf{V_1}$ to $\mathbf{V_2}$ and $\mathbf{u_2}$ from $\mathbf{V_2}$ to $\mathbf{V_1}$. To find $\mathbf{u_1}$ and $\mathbf{u_2}$, a regularized cost function can be formulated as:

$$C = D(\mathbf{V_1}(\mathbf{T_{u_1(0.5)}}(\mathbf{x})), \mathbf{V_2}(\mathbf{T_{u_2(0.5)}}(\mathbf{x}))) + \alpha \mathrm{tr}(\nabla \mathbf{u_1}^T \nabla \mathbf{u_1})^2 + \alpha \mathrm{tr}(\nabla \mathbf{u_2}^T \nabla \mathbf{u_2})^2 \quad (1)$$

where D is a dissimilarity metric, $\mathbf{V_1}(\mathbf{T_{u_1(0.5)}}(\mathbf{x}))$ is the middle volume from $\mathbf{V_1}$, $\mathbf{V_2}(\mathbf{T_{u_2(0.5)}}(\mathbf{x}))$ is the middle volume from $\mathbf{V_2}$, α is a regularization weight, tr is the trace operator and $\mathrm{tr}(\nabla \mathbf{u}^T \nabla \mathbf{u})^2$ is a diffusion regularization term.

The intensity of the same tissue can vary in two ultrasound scans due to changes of the insonification angle and shadowing and enhancing artifacts. We therefore select NCC as the similarity metric, which is invariant to such intensity variations and further can be reliably computed over small patches. Instead of using $-\mathrm{NCC}$ as the dissimilarity metric, we use $-\mathrm{NCC}^2$ to employ quadratic optimization methods. Then we divide the volumes into small patches, calculating $-\mathrm{NCC}^2$ in each patch, and add the results up to generate a global cost:

$$D = -\frac{1}{N} \sum_{i=1}^{N} \rho_i^2 \quad (2)$$

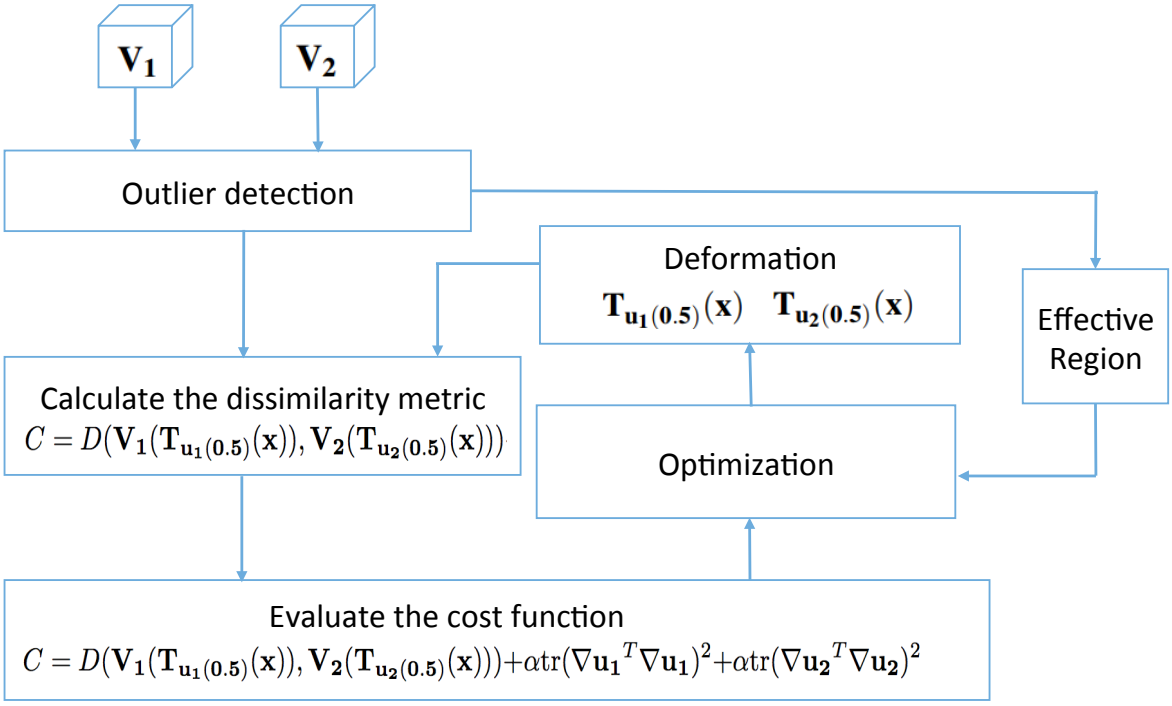

Fig. 1. Outline of the NSR registration technique.

$$\rho_i^2 = \frac{(\sum_{j=1}^{n}(V_{1j} - \overline{\mathbf{V_{1}}_i})(V_{2j} - \overline{\mathbf{V_{2}}_i}))^2}{\sum_{j=1}^{n}(V_{1j} - \overline{\mathbf{V_{1}}_i})^2 \sum_{j=1}^{n}(V_{2j} - \overline{\mathbf{V_{2}}_i})^2} \tag{3}$$

$$\mathbf{V_1} = \mathbf{V_1}(\mathbf{T_{u_1(0.5)}}(\mathbf{x})), \mathbf{V_2} = \mathbf{V_2}(\mathbf{T_{u_1(0.5)}}(\mathbf{x}))$$

where $\mathbf{V_{1}}_i$ and $\mathbf{V_{2}}_i$ are patch i in $\mathbf{V_1}$ and $\mathbf{V_2}$ respectively, V_{1j} and V_{2j} are the intensity of pixel j in patch i, $\overline{\mathbf{V_{1}}_i}$ and $\overline{\mathbf{V_{2}}_i}$ are the mean intensity of patch i, N is the number of patches in the volume and n is the number of pixels in each patch. The N patches are selected on a grid in image regions with high signal to noise ratios as elaborated in the next section.

B. Outlier Detection

During neurosurgery, brain tumors are resected and therefore do not correspond to resection cavities in post-resection ultrasound images. Obviously, missing correspondences undermine the effectiveness of our work. Therefore we develop a novel outlier detection approach to identify outliers and efficiently reduce the impact of non-correspondences between pre- and post-resection images.

In a recent work [30], we investigated the directions of derivatives of NCC in individual pixels in each iteration to detect outliers. We showed that these derivatives in non-corresponding regions pointed to random directions, while they generally pointed to the same direction in corresponding regions. These directions can be calculated using the vector $\frac{\partial \rho}{\partial \mathbf{u}}$ in each patch. Our new detection approach is based on this work, and further, we utilize an additional feature to improve the accuracy of detection. This feature is ρ, which is generally low for non-corresponding regions. Therefore, the metric r of a patch, which is used for outlier detection, is calculated using the following equations:

$$r_1 = \mathbf{std}(\frac{\partial \rho}{\partial \mathbf{u_1}}) - \beta \rho^2 \tag{4}$$

$$r_2 = \mathbf{std}(\frac{\partial \rho}{\partial \mathbf{u_2}}) - \beta \rho^2 \tag{5}$$

where β is a coefficient and $\mathbf{std}(\mathbf{v})$ is the standard deviation of the elements of vector $\mathbf{v}$. We will provide the analytic formula for $\frac{\partial \rho}{\partial \mathbf{u}}$ in Section III. This metric will be assigned to each pixel of that patch. If there are overlaps among patches, we will divide the sum of metrics in a pixel by the overlapping times. After doing this for all patches, a 3D volume whose size is the same as that of the ultrasound volume is constructed. We call this 3D volume "Initial Pattern". After setting a threshold for the "Initial Pattern", we treat elements whose value is greater than the threshold as outliers, and accordingly obtain a 3D binary volume showing corresponding (1) and non-corresponding (0) regions. This volume is composed of the information of outliers, which will be useful in the registration process. In addition to this mask, we construct a second volume wherein pixels with intensity less than 3% of the maximum intensity (i.e. with very low signal to noise ratio (SNR)) are assigned a value of 0. An "Effective Region" is obtained by combining these two volumes, where 0 pixels represent either outliers or regions suffering from low SNR. During registration, the dissimilarity metric will not be computed in regions of the "Effective Region" with zero values.

In order to validate the effectiveness of our outlier detection algorithm, we simulate our method on two images, which are shown in Fig. 2 (a) and (b). In this test, we only verify our

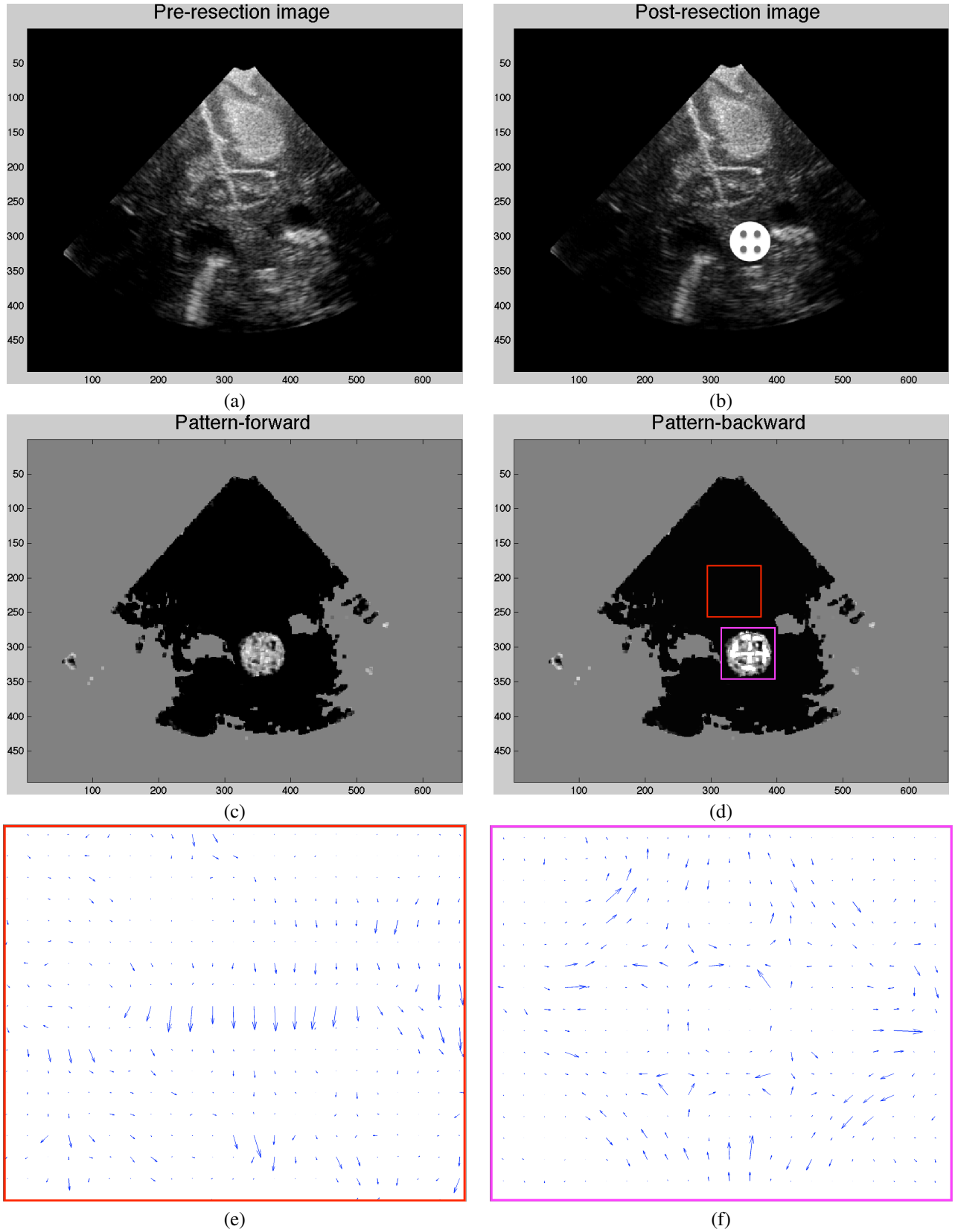

Fig. 2. Demonstration of the outlier detection technique. (a) is an image from the BITE database, while the contents in (b) are identical but displaced by 5 pixels in the vertical direction. The circular region in (b) represents an outlier region, simulating tissue resection. In pattern images (c) and (d), the black parts represent the regions with low metric, corresponding to inlier regions, whereas the bright parts indicate outlier regions. An inlier and an outlier patch are shown in (d) in red and magenta respectively. (e) and (f) show the Jacobian of NCC at each pixel in the inlier and outlier patches respectively.

outlier detection algorithm, without the registration process. The contents of these two images are identical, being displaced by five pixels in the vertical direction. The circular region in (b) represents an outlier region. After performing our outlier detection algorithm, we obtain the "Initial Pattern" in (c) and (d), wherein we can clearly and accurately distinguish outliers (non-corresponding regions) from inliers (corresponding regions). (e) and (f) demonstrate the Jacobian of NCC calculated at each pixel in an inlier patch and an outlier patch respectively. The location of the inlier patch and outlier patch is marked by red and magenta boxes in (d) respectively. As can be seen from these two images, pixels in the outlier patch generally move in random directions, whereas pixels in inlier regions move consistently. We repeated this experiment on 10 different pairs of ultrasound images and outlier patterns, and obtained similar results.

III. Optimization

To calculate the optimal deformation fields, we have to minimize the cost function. Usually, non-linear minimization problems are solved in an iterative manner. Several optimization algorithms can be applied to obtain incremental updates. Steepest gradient descent (SGD) is used in [23] to optimize the cost function. However, SGD always moves perpendicularly to isolines and generally has a low convergence rate [24]. The Gauss-Newton method can archive a quadratic convergence rate, but the cost function must be of a specific form. The Levenberg-Marquardt minimization method is indeed efficient for optimization. However since it is a mixture of the Gauss-Newton method and SGD, it has a convergence rate between linear and quadratic.

In this work, we use pseudo-inverse of the mean of Jacobian matrices as the optimization method, which is one of the ESM methods proposed in [24]. ESM uses first-order derivatives to approximate second-order derivatives, making optimization computationally efficient. In this algorithm, forward deformation Jacobian is combined with backward one to generate more accurate incremental updates. Despite the fact that ESM uses only first-order derivatives, it is shown to have a cubic convergence rate [31]. When we calculate $-\mathrm{NCC}^2$ in a patch, we can also obtain the value of NCC and the derivatives of NCC with respect to the intensity of each pixel in that patch. We assign the NCC to each pixel in that patch to act as the residual function:

$$\frac{\partial \rho_i}{\partial \mathbf{I}} = \frac{1}{|\mathbf{V_a}||\mathbf{V_b}|}(\mathbf{V_a} - \frac{\langle \mathbf{V_a}, \mathbf{V_b} \rangle}{|\mathbf{V_b}|^2}\mathbf{V_b}) \tag{6}$$

$$\mathbf{V_a} = \mathbf{V_{1}}_i - \overline{\mathbf{V_{1}}_i}, \mathbf{V_b} = \mathbf{V_{2}}_i - \overline{\mathbf{V_{1}}_i}$$

where ρ_i is the NCC of patch i and $\frac{\partial \rho_i}{\partial \mathbf{I}}$ is the derivative vector of NCC with respect to the intensity of each pixel in patch i. Since we need the NCC value and its derivative at each voxel, we define $\mathbf{P}$ as:

$$\mathbf{P} = \begin{bmatrix} \rho_1 & \rho_2 & \cdots & \rho_j & \cdots & \rho_M \end{bmatrix}^T \tag{7}$$

where ρ_j is the NCC value computed at pixel j and M is the total number of voxels in the volume. In an abuse of notation, we define $\frac{\partial \mathbf{P}}{\partial \mathbf{I}}$ as:

$$\frac{\partial \mathbf{P}}{\partial \mathbf{I}} = \begin{bmatrix} \frac{\partial \rho_1}{\partial I_1} & \frac{\partial \rho_2}{\partial I_2} & \cdots & \frac{\partial \rho_j}{\partial I_j} & \cdots & \frac{\partial \rho_M}{\partial I_M} \end{bmatrix}^T \tag{8}$$

where $\frac{\partial \rho_j}{\partial I_j}$ is the derivative of NCC in pixel j with respect to the intensity of that pixel. Note that some patches may have overlapping voxels. Using the chain rule, we obtain:

$$\nabla_{\mathbf{u_1}} \mathbf{P} = \frac{\partial \mathbf{P}}{\partial \mathbf{u_1}} = \frac{\partial \mathbf{I_{V_1}}}{\partial \mathbf{u_1}} \frac{\partial \mathbf{P}}{\partial \mathbf{I_{V_1}}} \tag{9}$$

$$\nabla_{\mathbf{u_2}} \mathbf{P} = \frac{\partial \mathbf{P}}{\partial \mathbf{u_2}} = \frac{\partial \mathbf{I_{V_2}}}{\partial \mathbf{u_2}} \frac{\partial \mathbf{P}}{\partial \mathbf{I_{V_2}}} \tag{10}$$

where $\frac{\partial \mathbf{I_V}}{\partial \mathbf{u}}$ is the gradient of intensity and $\nabla_{\mathbf{u_1}}$ and $\nabla_{\mathbf{u_2}}$ are the Jacobians with respect to forward and backward deformation fields respectively. Given the Jacobians of two directions, we can find the optimal deformation fields following an iterative rule. First the forward Jacobian is combined with the backward Jacobian to generate two average Jacobians, which will be used in the subsequent computation:

$$\nabla_{\mathbf{u_1}} \mathbf{P_{av}} = \frac{1}{2}(\nabla_{\mathbf{u_1}} \mathbf{P} - \nabla_{\mathbf{u_2}} \mathbf{P}) \tag{11}$$

$$\nabla_{\mathbf{u_2}} \mathbf{P_{av}} = \frac{1}{2}(\nabla_{\mathbf{u_2}} \mathbf{P} - \nabla_{\mathbf{u_1}} \mathbf{P}) \tag{12}$$

where $\nabla_{\mathbf{u_1}} \mathbf{P_{av}}$ and $\nabla_{\mathbf{u_2}} \mathbf{P_{av}}$ are average Jacobians for forward and backward deformations respectively. These two terms are denoted by $\nabla_{\mathbf{u_1}} \mathbf{P}$ and $\nabla_{\mathbf{u_2}} \mathbf{P}$ hereafter to prevent notation clutter. Incremental updates can then be computed with the rule $(\nabla_{\mathbf{u}} \mathbf{P}^T \nabla_{\mathbf{u}} \mathbf{P}) \mathbf{\Delta_u} = \nabla_{\mathbf{u}} \mathbf{P}^T \mathbf{P}$, where $\mathbf{P}$ is the vector of NCC (shown in Eq. 7) that acts as the residual function. Because of the diffusion regularization term, the update rule becomes [28]:

$$(\nabla_{\mathbf{u}} \mathbf{P}^T \nabla_{\mathbf{u}} \mathbf{P} + \alpha \mathbf{I}) \mathbf{\Delta_u} = \nabla_{\mathbf{u}} \mathbf{P}^T \mathbf{P} + \alpha \nabla^{\mathbf{2}} \mathbf{u_{previous}} \tag{13}$$

where $\mathbf{I}$ is an identity matrix, α is a coefficient and $\nabla^{\mathbf{2}} \mathbf{u_{previous}}$ is Laplacian of the sum of all previous updates. The incremental update $\mathbf{\Delta_u}$ is calculated using a successive over-relaxation solver. Compared with the Jacobi and Gauss-Seidel methods, it is more accurate and flexible for solving equations. Subsequently, deformation fields can be updated by adding the incremental updates:

$$\mathbf{u_1}^{t+1} = \mathbf{u_1}^t + \lambda \mathbf{\Delta_{u_1}} \tag{14}$$

$$\mathbf{u_2}^{t+1} = \mathbf{u_2}^t + \lambda \mathbf{\Delta_{u_2}} \tag{15}$$

where λ is a step size and $\mathbf{\Delta_{u_1}}$ and $\mathbf{\Delta_{u_2}}$ are incremental updates for forward and backward deformation fields respectively. Since we use the NCC vector as the residual function, whose elements approach one at the optimal alignment, we utilize a progressively smaller step size strategy. In each iteration, because of the symmetric and inverse-consistent registration, full deformation fields are calculated by:

$$\mathbf{u_{1\,full}} = \mathbf{u_1}(0.5) \circ \mathbf{u_2}(0.5)^{-1} \tag{16}$$

$$\mathbf{u_{2\,full}} = \mathbf{u_1}(0.5)^{-1} \circ \mathbf{u_2}(0.5) \tag{17}$$

Moreover, multi-level hierarchical registration from coarse to fine levels is applied in this work to speed up the registration process and avoid getting trapped in local minima.

IV. Experiments and Results

TO validate the performance of our outlier detection algorithm and our registration framework, pre- and post-resection ultrasound images of 13 patients are utilized from the BITE database [32]. The experimental procedures involving human subjects in BITE were approved by McGill University's Institutional Review Board. NSR takes approximately 40 seconds on a 3GHz processor to perform a typical 3D registration. These volumes are reconstructed from 2D ultrasound image sequences with the voxel size of $1\ mm \times 1\ mm \times 1\ mm$. And these datasets also include homologous anatomical landmarks in pre- and post-resection ultrasound volumes. The distribution of the landmarks of pre- and post-resection ultrasound volumes of one patient is shown in Fig. 3 as an example. To quantitatively measure the performance of NSR, we use the mean target registration errors (mTRE) metric, which shows the average distance between corresponding landmarks as follows. Let $\mathbf{x}$ and $\mathbf{x}'$ represent corresponding landmarks in $\mathbf{V_1}$ and $\mathbf{V_2}$ respectively, then mTRE can be calculated as [33]:

$$\mathrm{mTRE} = \frac{1}{n}\sum_{i}^{n} \|\mathbf{T_{u_1}}(\mathbf{x_i}) - \mathbf{x_i'}\| \tag{18}$$

where $\mathbf{T_{u_1}}$ is full forward deformation and n is the number of landmarks.

The original mTRE and final mTRE of all patients are shown in Table I. As can be seen from the table, every mTRE decreases after NSR registration. Even the mTRE of patient 11, whose initial value of 10.5 mm decreases to 2.8 mm after NSR. The distributions of mTRE and minimum TRE of RESOUND and NSR in Fig. 4 show that NSR provides a more outstanding registration result. This improvement is obtained by both improved optimization and the symmetric and inverse-consistent approach.

There are two important limitations in BITE TRE values. First, in average, around 9 landmarks are selected in each 3D volume, and therefore, the landmarks only show registration accuracy in a very small portion of ultrasound volumes. Second, manually selected landmarks in BITE are only accurate up to 1.58 mm [17] and 1.4 mm [30]. Therefore, to further demonstrate the effectiveness of our registration framework and our outlier detection algorithm, pre- and post-registration alignments of images of two patients are shown in Figs. 5 and 6. The results in these two patients are representative of the performance of NSR in all patients, and are selected for two reasons. First, ultrasound images have distinctive contours that clearly show the alignment quality. Second, tumors are large enough to be visible in ultrasound images, and therefore the quality of alignment can be assessed in regions close to non-corresponding regions that are hard to register. For completeness, the results of the remaining 11 patients are included in the supplementary material. To show the level of alignment between ultrasound images, we perform the following three steps: 1) Select an image from the pre-resection volume and the corresponding frame from the post-resection volume. 2) Automatically find edges of the pre-resection image using the Canny edge detection technique, and overlay the edges on the pre-resection frame in (a). 3) Overlay the edges of the pre-resection image on the post-resection frame in (b), which shows the misalignment between pre- and post-resection volumes. In (c) and (d), the post-resection images after registration with RESOUND and NSR are shown respectively. While better alignment with the pre-resection image is clear in both (c) and (d), NSR substantially outperforms RESOUND. Improved alignments with NSR (over RESOUND) are pointed by magenta arrows in (d) and red arrows in (c) respectively. Such qualitative results have significant advantages over mTRE because they show the level of alignment over a much larger region, compared with few points used in mTRE (around 9/patient). Parts (e) and (f) show the "Effective Region" for both directions, where the regions inside the yellow contour are treated as inliners and all the other regions are deemed as outliers or low SNR regions. Parts (g) and (h) are overlay of the contour of "Effective Region" on the corresponding frame of the volume, and we use these pictures to demonstrate the effectiveness of our outlier detection algorithm. The results show that NSR can identify outliers and low SNR regions and register these challenging images accurately and efficiently.

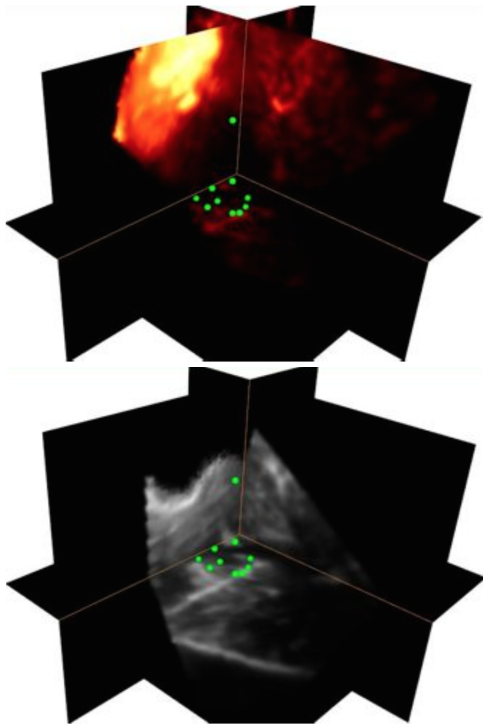

Fig. 3. Ten corresponding landmarks in pre- (top) and post-resection (bottom) ultrasound volumes.

TABLE I
MTRE VALUES BEFORE AND AFTER REGISTRATION WITH RESOUND AND NSR. LGG AND HGG REPRESENT LOW AND HIGH GRADE GLIOMA RESPECTIVELY. THE RESOUND DATA ARE FROM [23] AND ALL SMALLER VALUES ARE IN BOLD. THE p-VALUES IN THE LAST ROW SHOW THE STATISTICAL SIGNIFICANCE OF IMPROVEMENT OVER THE INITIAL MTRE.

Patient	Tumor type	Tumor size(cm^3)	Initial	RESOUND	NSR
P1	LGG	79.2	2.3(0.6-5.4)	1.8(0.5-4.0)	**1.4**(0.1-3.6)
P2	HGG	53.7	3.9(2.8-5.1)	1.4(0.5-1.9)	**1.2**(0.3-2.3)
P3	HGG	31.6	4.6(3.0-5.9)	1.4(0.7-2.2)	**1.2**(0.4-1.7)
P4	HGG	0.2	4.1(2.6-5.5)	1.2(0.3-2.4)	**1.1**(0.2-2.2)
P5	HGG	32.3	2.3(1.4-3.1)	**1.0**(0.2-1.7)	1.1(0.5-2.5)
P6	HGG	13.9	4.4(3.0-5.4)	**1.0**(0.4-1.7)	1.1(0.7-1.9)
P7	HGG	63.1	2.7(1.7-4.1)	1.7(0.9-3.6)	**1.4**(0.4-3.0)
P8	HGG	4.8	2.2(1.0-4.6)	1.4(0.6-3.2)	**1.3**(0.4-3.4)
P9	HGG	10.4	3.9(1.0-6.7)	**1.9**(0.7-4.1)	2.8(0.5-4.7)
P10	LGG	39.7	2.9(0.8-9.0)	2.2(0.6-5.3)	**2.2**(0.5-3.9)
P11	LGG	49.1	10.5(7.8-13.0)	**2.5**(1.1-4.2)	2.8(0.3-6.4)
P12	HGG	31.9	1.6(1.3-2.2)	**0.7**(0.2-1.6)	0.8(0.4-1.5)
P13	LGG	37.3	2.2(0.6-4.0)	**1.3**(0.2-2.8)	1.3(0.3-3.4)
mean	-	34.4	3.7(2.1-5.7)	**1.5**(0.5-3.0)	**1.5**(0.4-3.1)
p-value	-	-	-	0.0023	**0.0019**

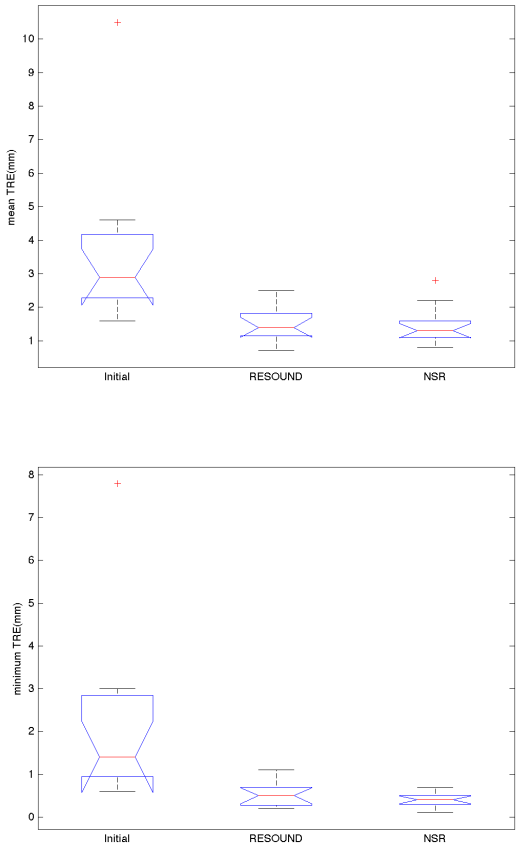

Fig. 4. Boxplots of the mean (top) and minimum (bottom) TRE.

V. CONCLUSION

A NOVEL robust framework is proposed in this paper for deformable registration of pre- and post-resection volumetric ultrasound images of neurosurgery. NCC, which is invariant to affine distortions of intensity values, is used as the similarity metric. ESM is used to optimize the regularized cost function to achieve fast and reliable registration. We use the symmetric and inverse-consistent approach to generate realistic deformation fields. Also, an outlier detection method is proposed and utilized to identify and locate non-corresponding regions. NSR outperforms RESOUND, as indicated in our results, for two main reasons: the improved deformation model and the more reliable optimization scheme. In future work we will investigate the parallel implementation of NSR to achieve real-time performance.

ACKNOWLEDGMENT

THIS project is funded by Natural Science and Engineering Research Council of Canada (NSERC) Discovery Grant RGPIN-2015-04136. We would like to thank anonymous reviewers for constructive feedback.

REFERENCES

[1] W. Stummer, U. Pichlmeier, T. Meinel, O. D. Wiestler, F. Zanella, H.-J. Reulen, ALA-Glioma Study Group *et al.*, "Fluorescence-guided surgery with 5-aminolevulinic acid for resection of malignant glioma: a randomised controlled multicentre phase iii trial," *The lancet oncology*, vol. 7, no. 5, pp. 392–401, 2006.

[2] A. Nabavi, P. M. Black, D. T. Gering, C.-F. Westin, V. Mehta, R. S. Pergolizzi Jr, M. Ferrant, S. K. Warfield, N. Hata, R. B. Schwartz *et al.*, "Serial intraoperative magnetic resonance imaging of brain shift," *Neurosurgery*, vol. 48, no. 4, pp. 787–798, 2001.

[3] G. Unsgård, O. Solheim, F. Lindseth, and T. Selbekk, *Intra-operative imaging with 3D ultrasound in neurosurgery*. Springer, 2011.

[4] O. Solheim, T. Selbekk, A. S. Jakola, and G. Unsgård, "Ultrasound-guided operations in unselected high-grade gliomas—overall results, impact of image quality and patient selection," *Acta neurochirurgica*, vol. 152, no. 11, pp. 1873–1886, 2010.

[5] M. A. El Beltagy, M. Aggag, and M. Kamal, "Role of intraoperative ultrasound in resection of pediatric brain tumors," *Child's Nervous System*, vol. 26, no. 9, pp. 1189–1193, 2010.

[6] M. Renovanz, A.-K. Hickmann, C. Henkel, M. Nadji-Ohl, and N. J. Hopf, "Navigated versus non-navigated intraoperative ultrasound: is there any impact on the extent of resection of high-grade gliomas? a retrospective clinical analysis." *Journal of neurological surgery. Part A, Central European neurosurgery*, vol. 75, no. 3, pp. 224–230, 2014.

[7] A. K. Petridis, M. Anokhin, J. Vavruska, M. Mahvash, and M. Scholz, "The value of intraoperative sonography in low grade glioma surgery," *Clinical neurology and neurosurgery*, vol. 131, pp. 64–68, 2015.

[8] J. Coburger, A. Scheuerle, D. R. Thal, J. Engelke, M. Hlavac, C. R. Wirtz, and R. König, "Linear array ultrasound in low-grade glioma surgery: histology-based assessment of accuracy in comparison to conventional intraoperative ultrasound and intraoperative mri," *Acta neurochirurgica*, vol. 157, no. 2, pp. 195–206, 2015.

[9] A. V. Moiyadi and P. Shetty, "Direct navigated 3d ultrasound for resection of brain tumors: a useful tool for intraoperative image guidance," *Neurosurgical Focus*, vol. 40, no. 3, p. E5, 2016.
[10] T. Selbekk, A. S. Jakola, O. Solheim, T. F. Johansen, F. Lindseth, I. Reinertsen, and G. Unsgård, "Ultrasound imaging in neurosurgery: approaches to minimize surgically induced image artefacts for improved resection control," *Acta neurochirurgica*, vol. 155, no. 6, pp. 973–980, 2013.
[11] J. A. Zagzebski, "Essentials of ultrasound physics," 1996.
[12] P. Foroughi, P. Abolmaesumi, and K. Hashtrudi-Zaad, "Intra-subject elastic registration of 3d ultrasound images," *Medical image analysis*, vol. 10, no. 5, pp. 713–725, 2006.
[13] R. J. Schneider, D. P. Perrin, N. V. Vasilyev, G. R. Marx, J. Pedro, and R. D. Howe, "Real-time image-based rigid registration of three-dimensional ultrasound," *Medical image analysis*, vol. 16, no. 2, pp. 402–414, 2012.
[14] I. Reinertsen, F. Lindseth, C. Askeland, D. H. Iversen, and G. Unsgård, "Intra-operative correction of brain-shift," *Acta neurochirurgica*, vol. 156, no. 7, pp. 1301–1310, 2014.
[15] V. Grau, H. Becher, and J. A. Noble, "Registration of multiview real-time 3-d echocardiographic sequences," *IEEE Transactions on Medical Imaging*, vol. 26, no. 9, pp. 1154–1165, 2007.
[16] K. Rajpoot, J. A. Noble, V. Grau, C. Szmigielski, and H. Becher, "Multiview rt3d echocardiography image fusion," in *Functional Imaging and Modeling of the Heart*. Springer, 2009, pp. 134–143.
[17] L. Mercier, D. Araujo, C. Haegelen, R. F. Del Maestro, K. Petrecca, and D. L. Collins, "Registering pre-and postresection 3-dimensional ultrasound for improved visualization of residual brain tumor," *Ultrasound in medicine & biology*, vol. 39, no. 1, pp. 16–29, 2013.
[18] B. Presles, M. Fargier-Voiron, M.-C. Biston, R. Lynch, A. Munoz, H. Liebgott, P. Pommier, S. Rit, and D. Sarrut, "Semiautomatic registration of 3d transabdominal ultrasound images for patient repositioning during postprostatectomy radiotherapy," *Medical physics*, vol. 41, no. 12, p. 122903, 2014.
[19] T. O'Shea, J. Bamber, and E. Harris, "Mo-de-210-05: Improved accuracy of liver feature motion estimation in b-mode ultrasound for image-guided radiation therapy," *Medical physics*, vol. 42, no. 6, pp. 3560–3560, 2015.
[20] J. Banerjee, C. Klink, E. D. Peters, W. J. Niessen, A. Moelker, and T. van Walsum, "Fast and robust 3d ultrasound registration–block and game theoretic matching," *Medical image analysis*, vol. 20, no. 1, pp. 173–183, 2015.
[21] Y. Gao, J. Ma, J. Zhao, J. Tian, and D. Zhang, "A robust and outlier-adaptive method for non-rigid point registration," *Pattern Analysis and Applications*, vol. 17, no. 2, pp. 379–388, 2014.
[22] A. Khamene, D. Zikic, M. Diallo, T. Boettger, and E. Rietzel, "A novel intensity similarity metric with soft spatial constraint for a deformable image registration problem in radiation therapy," in *Medical Image Computing and Computer-Assisted Intervention–MICCAI 2009*. Springer, 2009, pp. 828–836.
[23] H. Rivaz and D. L. Collins, "Near real-time robust non-rigid registration of volumetric ultrasound images for neurosurgery," *Ultrasound in medicine & biology*, vol. 41, no. 2, pp. 574–587, 2015.
[24] E. Malis, "Improving vision-based control using efficient second-order minimization techniques," in *ICRA'04. 2004 IEEE International Conference on Robotics and Automation*, vol. 2. IEEE, 2004, pp. 1843–1848.
[25] H. Zhou and H. Rivaz, "Robust deformable registration of pre-and post-resection ultrasound volumes for visualization of residual tumor in neurosurgery," in *Engineering in Medicine and Biology Society (EMBC), 2015 37th Annual International Conference of the IEEE*. IEEE, 2015, pp. 141–144.
[26] G. E. Christensen and H. J. Johnson, "Consistent image registration," *IEEE Transactions on Medical Imaging*, vol. 20, no. 7, pp. 568–582, 2001.
[27] D. Shen and C. Davatzikos, "Hammer: hierarchical attribute matching mechanism for elastic registration," *IEEE Transactions on Medical Imaging*, vol. 21, no. 11, pp. 1421–1439, 2002.
[28] M. P. Heinrich, M. Jenkinson, M. Bhushan, T. Matin, F. V. Gleeson, M. Brady, and J. A. Schnabel, "Mind: Modality independent neighbourhood descriptor for multi-modal deformable registration," *Medical Image Analysis*, vol. 16, no. 7, pp. 1423–1435, 2012.
[29] M. Chen, W. Lu, Q. Chen, K. J. Ruchala, and G. H. Olivera, "A simple fixed-point approach to invert a deformation field," *Medical physics*, vol. 35, no. 1, pp. 81–88, 2008.
[30] H. Rivaz, S. J.-S. Chen, and D. L. Collins, "Automatic deformable mr-ultrasound registration for image-guided neurosurgery," *IEEE Transactions on Medical Imaging*, vol. 34, no. 2, pp. 366–380, 2015.
[31] E. Malis, "Vision-based estimation and robot control," Ph.D. dissertation, Université Nice Sophia Antipolis, 2008.
[32] L. Mercier, R. F. Del Maestro, K. Petrecca, D. Araujo, C. Haegelen, and D. L. Collins, "Online database of clinical mr and ultrasound images of brain tumors," *Medical physics*, vol. 39, no. 6, pp. 3253–3261, 2012.
[33] P. Jannin, J. M. Fitzpatrick, D. Hawkes, X. Pennec, R. Shahidi, and M. Vannier, "Validation of medical image processing in image-guided therapy." *IEEE Transactions on Medical Imaging*, vol. 21, no. 12, pp. 1445–1449, 2002.

Hang Zhou received his B.Sc. degree in communication engineering from Shenyang University of Technology, Shenyang, China, in 2013. He is currently pursuing his M.A.Sc. degree in electrical and computer engineering at Concordia University, Montreal, Canada.

His research interests include ultrasound imaging, registration of ultrasound images in neurosurgery and motion tracking in radiotherapy.

Hassan Rivaz received his B.Sc. from Sharif University of Technology, his M.A.Sc. from University of British Columbia, and his Ph.D. from Johns Hopkins University. He did a post-doctoral training at McGill University.

Since 2014, he has been an Assistant Professor at the Department of Electrical and Computer Engineering and the PERFORM Centre at Concordia University, where he is directing the IMPACT Group: Image Processing and Characterization of Tissue.

His main research interests are medical image processing, ultrasound elastography, registration, segmentation and machine learning. Clinical applications of his work are in neurosurgery, liver surgery, breast radiotherapy, prostatectomy and musculoskeletal diagnosis.

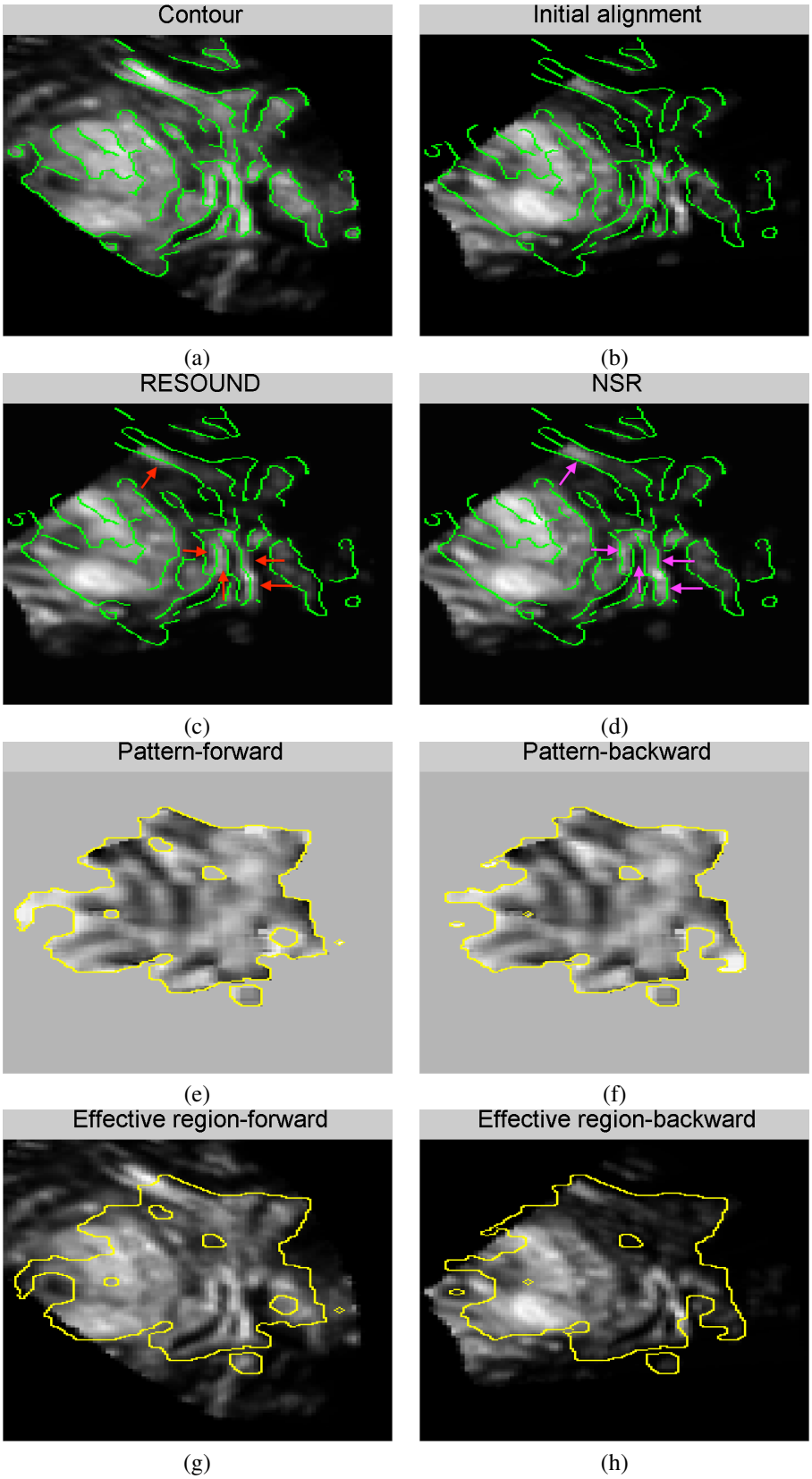

Fig. 5. Registration results of Patient 2. Please refer to the text for details.

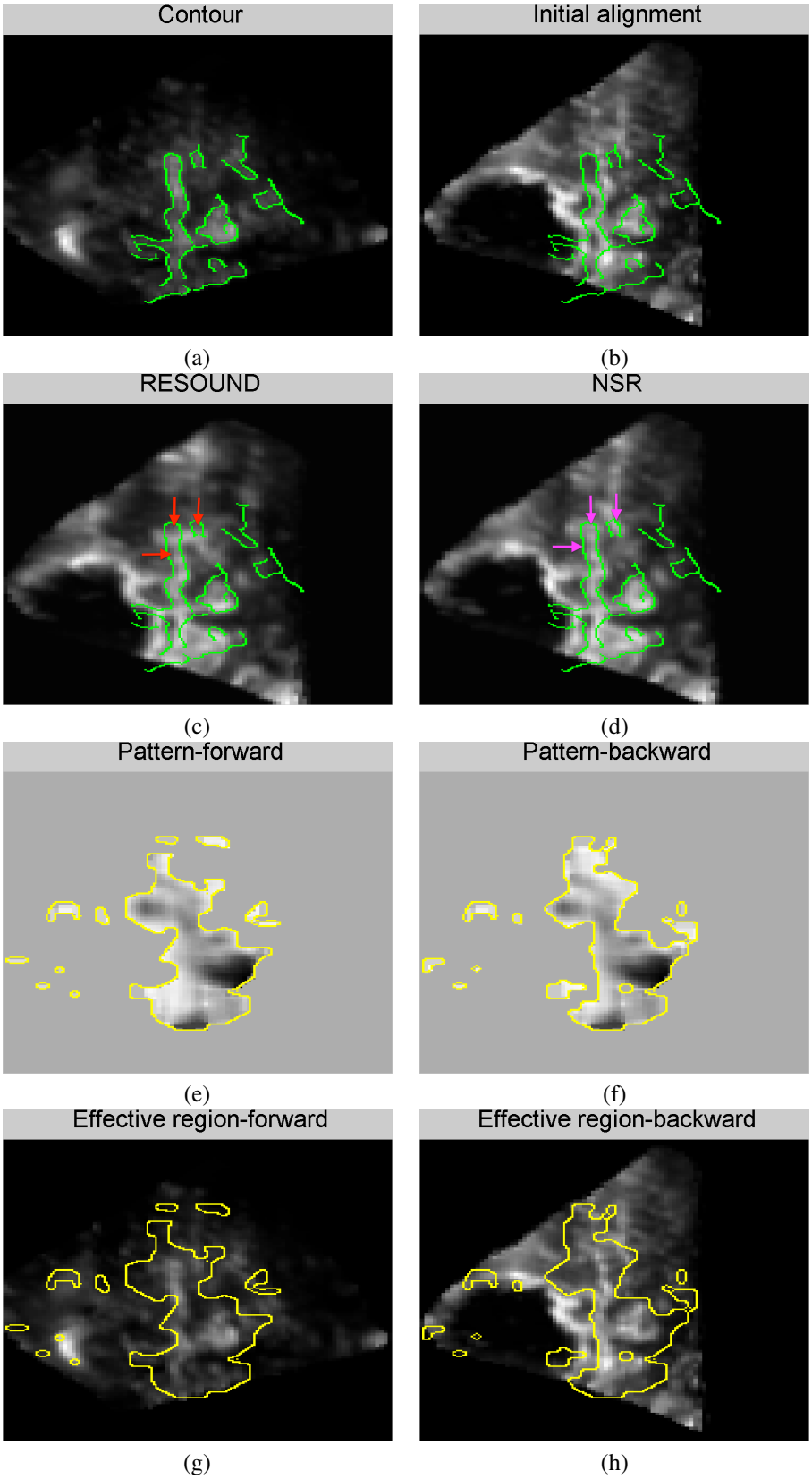

Fig. 6. Registration results of Patient 4. Please refer to the text for details.